Ecotoxicology and Environmental Safety 254 (2023) 114728

Contents lists available at ScienceDirect

Ecotoxicology and Environmental Safety

journal homepage: www.elsevier.com/locate/ecoenv

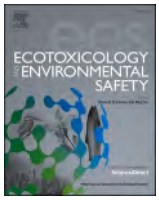

Efficient removal of Tris(2-chloroethyl) phosphate by biochar derived from shrimp shell: Adsorption performance and mechanism study

Chenyu Yang [a,b], Chang Liu [b], Yile Yan [b], Lun Lu [b], Ruixue Ma [b], Xian Xiao [a,*], Yang Yu [c], Yuan Zhao [a], Yunjiang Yu [b], Liangzhong Li [b,*]

[a] School of Environment & Safety Engineering, ChangZhou University, Changzhou 213164, China
[b] State Environmental Protection Key Laboratory of Environmental Pollution Health Risk Assessment, Center for Environmental Health Research, South China Institute of Environmental Sciences, The Ministry of Ecological and Environment of China, Guangzhou 510655, China
[c] Guangdong Key Laboratory of Environmental Pollution and Health, School of Environment, Jinan University, Guangzhou 511443, China

ARTICLE INFO

Keywords:
Tris(2-chloroethyl) phosphate
Shrimp shell biochar
Adsorption
Mechanism

ABSTRACT

Tris(2-chloroethyl) phosphate (TCEP) has been detected all over the world as a typical refractory organic phosphate, especially in groundwater. This work applied a calcium-rich biochar derived from shrimp shell as a low-cost adsorbent for TCEP removal. Based on the kinetics and isotherm studies, the adsorption of TCEP on biochar was monolayer adsorbed on a uniform surface, with SS1000 (the biochar was prepared at the carbonization temperature of 1000 °C) achieving the maximum adsorption capacity of 264.11 mg·g^{-1}. The prepared biochar demonstrated stable TCEP removal ability throughout a wide pH range, in the presence of co-existing anions, and in diverse water bodies. A rapid removal rate of TCEP was observed during the adsorption process. When the dosage of SS1000 was 0.2 g·L^{-1}, 95% of TCEP could be removed within the first 30 min. The mechanism analysis indicated that the calcium species and basic functional groups on the SS1000 surface were highly involved in the TCEP adsorption process.

1. Introduction

About 93 billion tons of crustaceans comprising shrimp, prawns, and lobsters are produced globally per year (Mathew et al., 2020). Around 45–48% of shrimp shells (body carapace and head) are discarded as waste, to explore the application of shrimp shells in other fields is urgently needed to meet the sustainable development requirement and normal operation of shrimp and processing industries (Tseng et al., 2022). The pyrolysis procedure has been applied for reducing the volume and mass of biomass materials and simultaneously producing biochar (Dai et al., 2021; Hamid et al., 2022). Benefiting for excellent physicochemical properties such as large specific surface area and abundant oxygen-containing functional groups, the biochar has been widely used in applications such as soil remediation, wastewater treatment and carbon sequestration (Ji et al., 2023; Li et al., 2022). Various biomass materials like coconut shell, wood chips, corn cobs, and straw have been used to prepare biochar (Lei et al., 2022; Tang et al., 2021). In comparison, shrimp shell is rich in calcium, protein, and as a carbon source, they can produce biochar with residual calcium and nitrogen (Long et al., 2017; Xiao et al., 2017). The presence of calcium in biochar could provide more active sites for the adsorption of organic pollutants according to the literature (Dai et al., 2017, 2018). Hence, the utilization of shrimp shell waste as the source of biochar that has prosing application potential on water treatment could be a two-birds-one-stone strategy for resource recycling and environmental protection.

Flame Retardants (FRs) are commonly used in varnishes, polyurethane foams, plastics, electronic equipment, wood, textiles and other chemicals (Sunderland et al., 2019). Due to the strict restriction of polybrominated diphenyl ethers (PBDEs) and polychlorinated biphenyls (PCBs) as flame retardants in Europe and the USA (Lenters et al., 2019), their alternatives (e.g., organophosphorus flame retardants (OPFRs)) have been widely applied in various industries (Li et al., 2019). Global annual consumption of FRs exceeds 2 million tons, with OPFRs accounting for 16%, and will continue to grow at an annualized rate of 3.4%. However, OPFRs are not as safe as expected. Tris(2-chloroethyl) phosphate (TCEP), for example, has been proven to be neurotoxic (Sala et al., 2019), reproductive toxic (Hao et al., 2020) and carcinogenic (Zhang et al., 2021). Since TCEP is mainly added to products in a

* Corresponding authors.
E-mail addresses: xiaoxianivy@163.com (X. Xiao), liliangzhong@scies.org (L. Li).

https://doi.org/10.1016/j.ecoenv.2023.114728
Received 8 November 2022; Received in revised form 21 February 2023; Accepted 2 March 2023

simple physical form, it is readily released into the surrounding environment (van der Veen and de Boer, 2012). So far, TCEP has been detected in wastewater (Li et al., 2021c), marine (Zheng et al., 2022), river (Han et al., 2021), groundwater (He et al., 2022a) and drinking water (Zhu et al., 2022) all around the world. Groundwater contributes one-third of the country's water resources, and 70% of the population in China relies on it (He et al., 2022b). TCEP contamination in groundwater has posed a significant risk to human health (An et al., 2017; Jiang et al., 2019). Therefore, effective technologies for the efficient removal of TCEP from groundwater are urgently needed. TCEP is chemically stable, highly water soluble, difficult to degrade naturally and poorly biodegradable, and tends to remain in anaerobic, non-light and oligotrophic groundwater (Gerrity et al., 2012; Luo et al., 2014; Reemtsma et al., 2008). The currently screened strain TCM1 Rhizobium requires cultivation under aerobic conditions for better TCEP degradation (Zhou et al., 2020), and commonly used oxidants such as H_2O_2 (Liu et al., 2020), TiO_2 (Abdullah and O'Shea, 2019) and persulfate (Yu et al., 2021) can degrade TCEP with the assistance of UV light. Biological treatment and advanced oxidation techniques were found to be difficult for significant removal of TCEP from groundwater with the anaerobic, light-free and oligotrophic features (Choi and Kim, 2021; Lee et al., 2016). In comparison, adsorption can be considered as an effective and economical method of removing pollutants from water (Dardouri et al., 2018; Liang et al., 2018), but studies on TCEP removal by adsorption are very limited in the literature. Biochar has been proven to be a strong adsorbent for aromatic organic pollutants such as polycyclic aromatic hydrocarbons, pesticides and phthalates benefiting from its high surface hydrophobicity, large surface area and rich aromatic composition (Cai et al., 2021; Dou et al., 2022; Jin et al., 2016). As a result, it is reasonable to assume that the biochar derived from shrimp shell may have a high adsorption affinity for TCEP as aromatic organophosphate esters.

Herein, a biochar derived from shrimp shell was prepared through oxygen-limited pyrolysis method and used as the adsorbent for TCEP removal from water. The performance of biochar on TCEP removal was optimized by changing the pyrolysis temperature. The adsorption kinetics and isotherm of TCEP on the optimized biochar were studied. The effects of initial pH, co-existing ions and different water matrices on the removal of TCEP were clarified through batch experiments. The probable mechanism of TCEP removal was elucidated as well. This work provided a two-birds-one-stone strategy for the disposal of shrimp shell waste and development of biochar with promising application potential on TCEP removal from water.

2. Materials and methods

2.1. Chemical and reagents

Shrimp shell (SS) were collected from a shrimp processing factory located in Wenzhou, China. Tris(2-chloroethyl) phosphate (TCEP, >98%), Triphenyl phosphate (TPhP, 99%), bisphenol (BPA, 99%), tetrabromobisphenol A (TBBPA, 99%), hydrochloric acid (HCl, 37%), ammonium acetate (CH_3COONH_4, 99%), sodium chloride (NaCl, 98%), sodium bicarbonate ($NaHCO_3$, 98%), sodium dihydrogen phosphate (NaH_2PO_4, 98%), humic acid (HA, 90%) were purchased from Macklin, China. Deionized water (>18 mΩ·cm, Milli-Q systems) obtained from a lab-scale Milli-Q system was used for the solution preparation.

2.2. Preparation of biochar

The SS was washed, dried in an oven and crushed into fine powders smaller than 0.20 mm in size. The collected powders were pyrolyzed for 2 h in a tubular furnace at 600 °C, 800 °C, 1000 °C and 1200 °C under a continuous flow of nitrogen respectively. The carbonized powder as SS biochar was successively washed with water and ethanol five times before drying them dried at 60 °C for 10 h. The obtained biochars (SSs) were named SS600, SS800, SS1000, and SS1200 based on their carbonization temperatures.

2.3. Characterization of biochar

Specific surface area and pore size distribution of the biochar were detected by Micromeritics ASAP 2460 (USA). The surface morphology of the biochar was observed by scanning electron microscopy (SEM, Zeiss Gemini 500, Germany). The X-ray diffraction pattern (XRD) was recorded by Japan Rigaku Ultima IV with Cu Kα radiation. X-ray photoelectron spectroscopy (XPS, Thermo Scientific, USA) was performed to analyze the surface composition and valence states of different elements in SSs. Fourier transform infrared spectrometer (FT-IR, Nicolet iS 10, USA) was employed to detect the functional groups on the biochar surface in the wavenumber range of 650–4000 cm^{-1}. Boehm titration was used to quantitatively determine basic functional groups (BFG) on the biochar surface (Chingombe et al., 2005). The point of zero charge (pH_{PZC}) of the biochar was determined by an immersion technique (Tripathy and Kanungo, 2005).

2.4. Experiments for TCEP removal

To simulate a groundwater environment, the experimental solutions were de-oxygenated by aerating nitrogen. The kinetics experiment was conducted at the TCEP concentration of 10 $mg{\cdot}L^{-1}$, biochar dosage of 0.10 $g{\cdot}L^{-1}$, and pH of 7.0. The adsorption isotherm was conducted at initial concentrations of TCEP from 1 to 120 $mg{\cdot}L^{-1}$. The effect of biochar dosage (0.05–0.20 $g{\cdot}L^{-1}$), initial solution pH (3.0–11.0, adjusted with 0.1 M H_2SO_4 and 0.1 M NaOH), coexisting substances (Cl^-, HCO_3^-, $H_2PO_4^-$, and HA), and different water environment (groundwater, river water, and dye effluent) in the TCEP removal was investigated to assess the TCEP removal performance of the prepared biochar. Following the experiment, samples were filtered with a 0.22 μm syringe filter before the TCEP concentration measurement and detect BCEP (bis(2-chloroethyl) phosphate) using LC-MS/MS (Applied Biosystems, USA). The detailed procedure was provided in Text S1. Most of experiments were conducted in triplicates, and the mean values with standard deviations were presented in the Figures.

3. Results and discussion

3.1. Characterization

The surface morphology of SSs prepared at different carbonation temperatures was observed by SEM, which can be seen in Fig. 1 and S1. The formed biochar bulk was found to be covered by irregular nanoparticles, including flakes, spheres and rods. Fig. S2 depicts an IV-type isothermal curve as well as a large H4-type hysteretic loop of the desorption branch visible from the SSs, indicating the characteristic of mesoporous and stack structure of the slit pores (Ye et al., 2020). Especially, the number of the attached nanoparticles increased as the carbonization temperature climbed from 600 °C to 1200 °C, resulting in a reduction in pore volume from 0.36 to 0.26 $cm^3{\cdot}g^{-1}$. This is consistent with the result of BET analysis that the SS800 had a higher special surfacer area of 408.10 $m^2{\cdot}g^{-1}$ than the SS1000 (296.70 $m^2{\cdot}g^{-1}$). In order to exploit the possible change in the crystal structure of SSs at different temperatures of pyrolysis, the XRD patterns of the prepared SSs were investigated and the results are given in Fig. 2a. All of the biochar exhibited a highly crystalline structure of CaO (2θ = 22.96°, 31.34°), $CaCO_3$ (2θ = 35.88°, 39.28°) and $Ca(OH)_2$ (2θ = 18.40°, 33.98°) (PDF#05–0586) (Dai et al., 2018). The intensity of the diffraction peaks corresponding to $CaCO_3$ gradually decreased, mainly due to the decomposition of $CaCO_3$ at higher pyrolysis temperatures. On the contrary, the intensity of the diffraction peaks corresponding to $Ca(OH)_2$ on SSs gradually increased, resulting from the transformation of CaO during the washing treatment process.

As shown in Fig. 2b, FT-IR was employed to analyze the composition

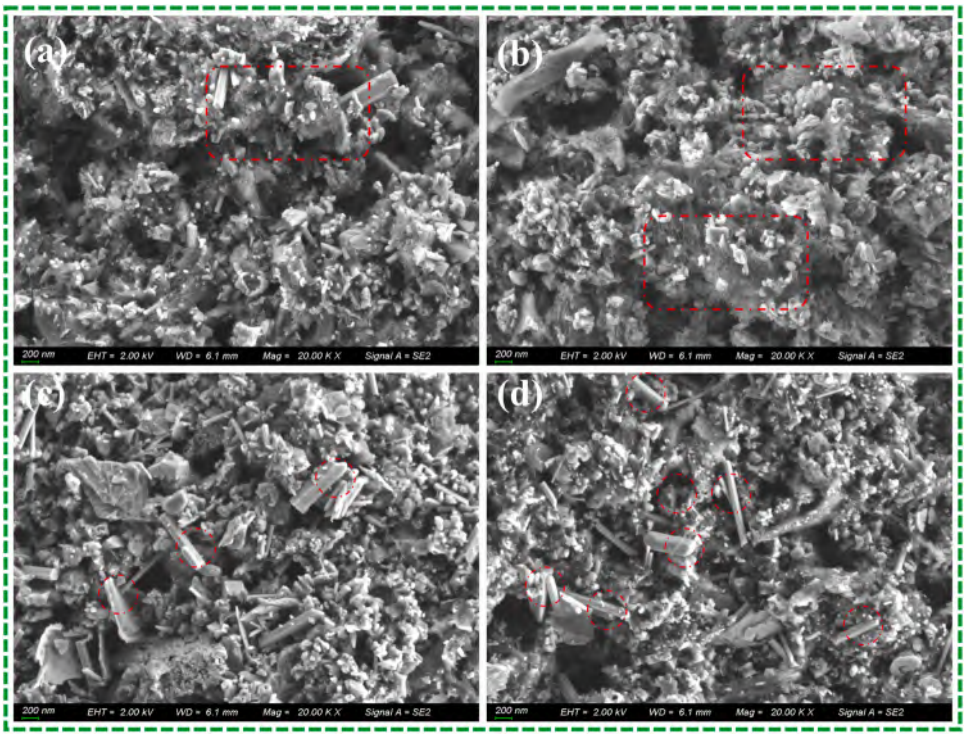

Fig. 1. SEM images. (a) SS600, (b) SS800, (c) SS1000, and (d) SS1200.

of surface functional groups on SSs. Based on the presence of characteristic peaks at 1404, 871, and 711 cm^{-1}, the formed SSs exhibit typical calcite spectra (Dai et al., 2017). The bands in the 2980–2920 cm^{-1} region are assigned to the stretching vibrations of CH, CH_2, and CH_3. The peak intensity at 3674 cm^{-1}, caused by the stretching vibration of Ca $(OH)_2$ became noticeably stronger with increasing the carbonization temperature. It is worth noting that attributed to C-O stretching vibration or O-H, the band intensity at 1066 cm^{-1} on SSs also increased at the higher carbonization temperature. The composition of carbon or oxygen-based functional groups was exploited by XPS analysis as shown in Fig. 2c and d. The core-level C 1 s spectra could be decomposed into three component peaks with the binding energies of 284.80, 285.48, and 289.48 eV, corresponding to graphitic C, C-O, and C═O. For the core-level O 1 s, the presence of three peaks with binding energies of 531.48, 532.27, and 533.28 eV are ascribed to C-O, ketonic C═O groups and hydroxyl C-O-H groups, respectively. Noticeably, that the content of hydroxyl C-O-H groups that existed in SS1000 and SS1200 rose when the carbonization temperature went up. In contrast, it was hardly detected in SS600 and SS800, which fits the FT-IR results well. Since the surface charge of the SSs is crucial for their adsorption performance, the point of zero charge (pH_{PZC}) of SSs was calculate. The pH_{PZC} values of SS600–1200 are about 7.1, 7.3, 8.0 and 8.2, accordingly. A higher pH_{PZC} refers to more basic functional groups (BFG) on the SSs surface (Dai et al., 2017; Tian et al., 2022). Based on the Boehm experiment results, the BFG on the surface of SS600–1200 was 1.29, 1.72, 3.13 and, 3.35 $mmol{\cdot}L^{-1}$.

3.2. Kinetics and isotherm study

The adsorption rate of TECP onto SS600–1200 was investigated by the pseudo-first-order, pseudo-second-order and intraparticle diffusion models expressed in Eqs. (1)–(3), and the results are presented in Fig. 3a, b. The corresponding paraments are illustrated in Table S2. According to Fig. 3a, the adsorption equilibrium time of TCEP on SS600, SS800, SS1000 and SS1200 was reached at 2 h, 1 h, 0.5 h and 0.5 h, respectively. Compared to the pseudo-first-order model, the pseudo-second-order model better simulated the experimental data, suggesting that the TCEP adsorption is controlled by the chemosorption process. Similar findings were also reported for the adsorption of methyl orange, Congo red and bisphenol A on shrimp shell based biochar (He et al., 2020; Zafar et al., 2022; Zhou et al., 2018). As seen from the modeling results in Fig. 3b and Table S3, the intraparticle diffusion process of TCEP exhibited multilinearity. The linear tendency with the rate constant (from 0.52 $mg{\cdot}g^{-1}{\cdot}min^{-1/2}$ to 13.93 $mg{\cdot}g^{-1}{\cdot}min^{-1/2}$) corresponds to the intraparticle diffusion process, while the one with much lower rate constant (from 0.19 $mg{\cdot}g^{-1}{\cdot}min^{-1/2}$ to 0.56 $mg{\cdot}g^{-1}{\cdot}min^{-1/2}$) reflects the adsorption equilibrium process in which the dramatic reduction of the rate constant is caused by the decreased TCEP concentration gradient in water. Thus, the adsorption rate of TCEP would be mainly dominated by the intraparticle diffusion process. Combined with the results of SEM and BET analysis, the biochar with higher special surface area exhibited a more significant intraparticle diffusion process. For SS1000, the boundary layer effect indicator C was 6.27 $mg{\cdot}L^{-1}$, which equals 9.86% of the equilibrium adsorption capacity. This indicates that the effect boundary layer on the TCEP adsorption is far lower than other carbon-based adsorbent (Tang et al., 2021; Tong et al., 2020; Zhang et al., 2022).

$$Q_t = Q_e\left(1 - e^{-k_1 t}\right) \tag{1}$$

$$Q_t = \frac{k_2 Q_e^2 t}{1 + k_2 Q_e t} \tag{2}$$

$$Q_t = k_i t^{\frac{1}{2}} + C \tag{3}$$

where Q_e and Q_t ($mg{\cdot}g^{-1}$) are the adsorption amounts biochar to of TCEP at equilibrium and at time t, respectively; k_1 (min^{-1}) and k_2 ($mg{\cdot}g^{-1}{\cdot}min$) are the Kinetic constants of pseudo- first-order, pseudo-second-order, respectively; k_i ($mg{\cdot}g^{-1}{\cdot}min^{-1/2}$) is the intraparticle diffusion model constant; C is related to the thickness and boundary layer of the adsorbent.

To further reveal the mutual effects between TCEP and SSs, the adsorption isotherms study described in Eqs. (4)–(5) was performed,

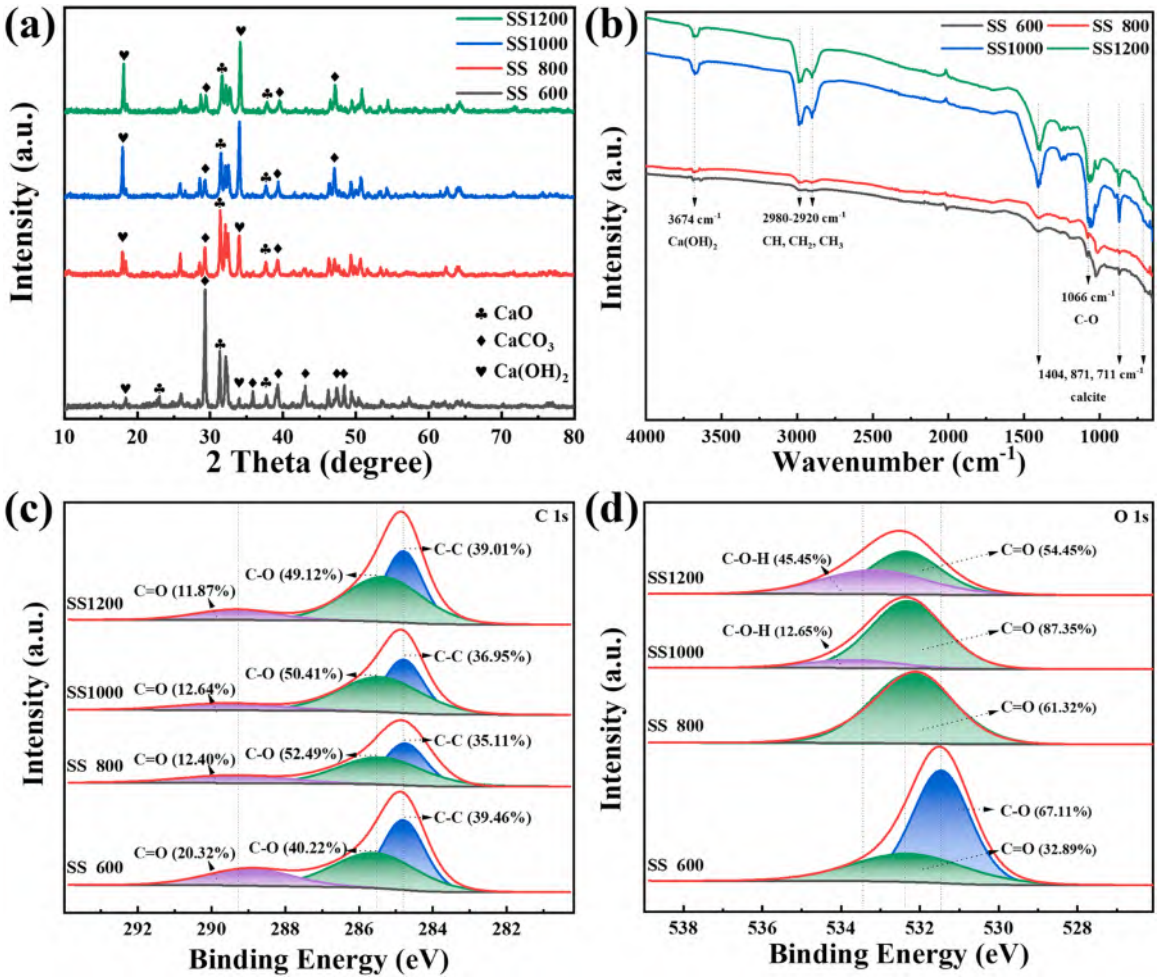

Fig. 2. The (a) XRD patterns, and (b) FT-IR spectra, (c) the C 1 s XPS spectra and (d) the O 1 s spectra of SSs.

with the results shown in Fig. 3c, Table S4. The Langmuir isotherm model with a higher regression coefficient (R^2) value is more suitable for fitting the experimental data. This indicates that the interaction between TCEP and SSs is monolayer adsorption on a homogeneous surface (Li et al., 2021b; Tang et al., 2021). The maximum adsorption capacity of SS600, SS800, SS1000 and SS1200 is 17.30, 83.68, 264.11 and 287.47 mg·g^{-1}, respectively. The R_L values of TCEP adsorption on different SSs were calculated from the Langmuir isotherm to evaluate the adsorption favorability. The R_L values for all the SSs ranged between 0 and 1, suggesting the TCEP adsorption on SSs is a favorable process (Mironyuk et al., 2019).

$$Q_e = K_F C_e^{\frac{1}{n}} \tag{4}$$

$$Q_e = \frac{Q_{\max} K_L C_e}{1 + K_L C_e} \tag{5}$$

where C_e (mg·g^{-1}) is the concentration of TCEP in solution at equilibrium; K_F (μ·g$^{1-1/n}$·L$^{1/n}$·g^{-1}) and n are the Freundlich constants, and $Q_{\max}$ (mg·g^{-1}) and K_L (L·mg^{-1}) are the Langmuir constants representing the maximum adsorption capacity and the adsorption affinity between the biochar and the TCEP (Text S2).

3.3. Performance evaluation of SSs in removing TCEP

The SS1000 was chosen to evaluate the TCEP adsorption performance under different operational conditions such as solution pH, coexisting ions, adsorbent dosage, and water matric. The solution pH may affect the deprotonation or protonation of functional groups on biochar, and then cause an impact on the removal of adsorbates. As demonstrated in Fig. 3d, the SS1000 could achieve a stable removal capability (Q_e> 60 mg·g^{-1}) in the entire tested pH range of 3.0–11.0. For the control experiment in which no adsorbent was added, the negligible removal of TCEP is observed when the pH was below 8.0. With a further increase in solution pH, a small part of TCEP can be removed from the water, attributing to the self-hydrolysis of TCEP under such basic condition (Wu et al., 2018).

As depicted in Fig. 3e, when the low-concentration Cl^- ions (10 mM) was added into the solution, the adsorption of TCEP on SS1000 increased by about 3%. However, the TCEP removal was slightly hindered at high concentration of Cl^- ions (100 mM). This may be related to the salting-out effect, where the adsorption of organic pollutants on the adsorbent increases with the increase of ionic concentration. When the Cl^- ion concentration reaches a certain level, the neutralization of the surface charge may achieve more quickly due to the occupation the adsorption sites under stronger electrostatic gravitational forces, resulting in a decrease in TCEP adsorption on SS1000 (Liu et al., 2020). The enhanced removal of TCEP with the increase of HCO_3^- concentration may account for the basicity of HCO_3^- in aqueous solution, which can facilitate the self-hydrolysis process of TCEP and thus promote the removal of TCEP from water. $H_2PO_4^-$ in the solution affected the TCEP adsorption by SS1000 (Q_e> 50 mg·g^{-1}), probably due to the competition of the adsorption sites between SS1000 and TCEP (Ji et al., 2020). Humic acid (HA), as a representative of natural organic matter, can influence the removal of organic pollutants on carbon-based adsorbents. As shown in Fig. 3e, low-concentration HA had little effect on the

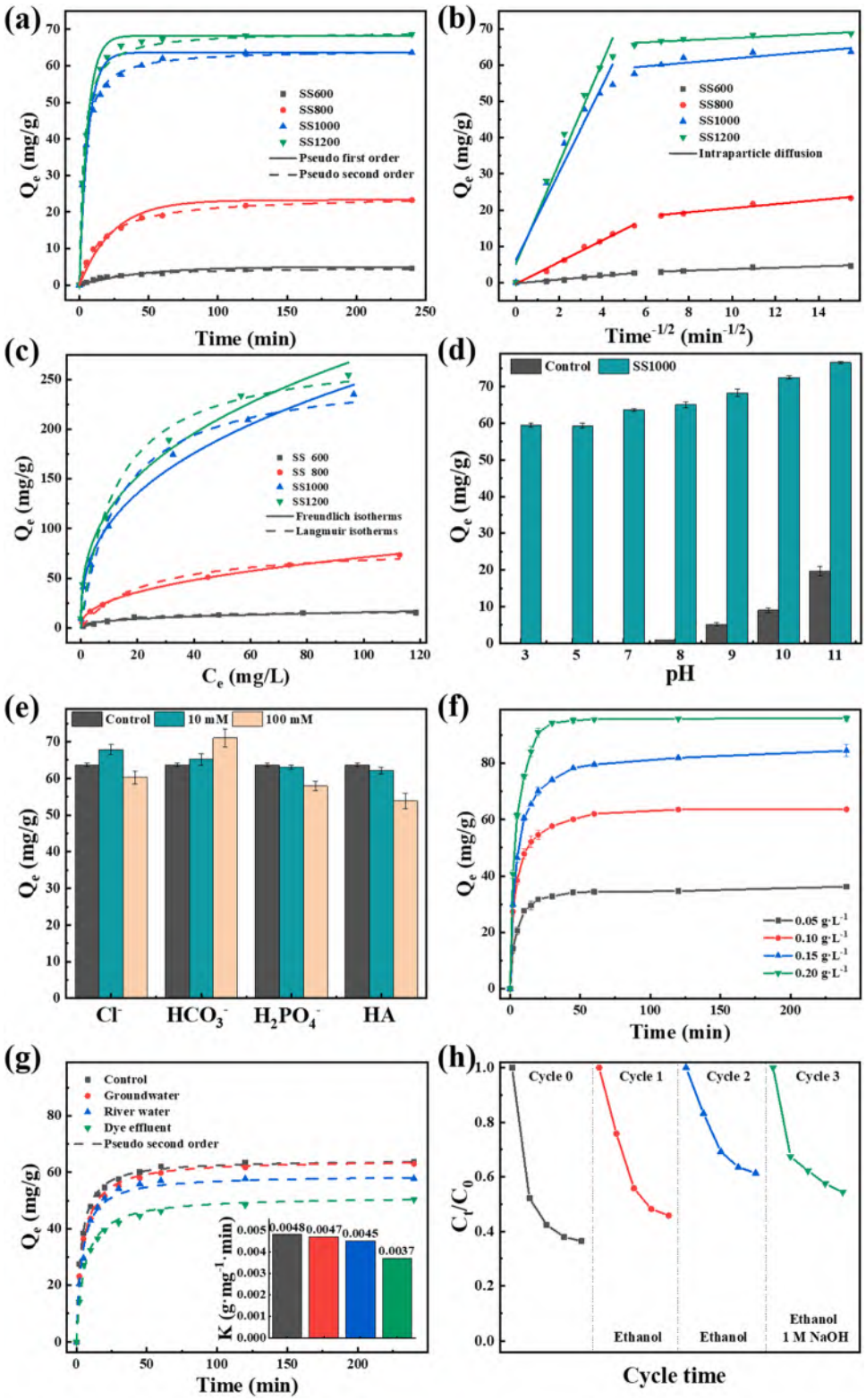

Fig. 3. Adsorption kinetics of TCEP on SSs with the fitting of (a) the pseudo-first-order and pseudo-second-order model and (b) the intraparticle diffusion model. Adsorption isotherms of TCEP on SSs (c). The different factors for TCEP adsorption on SS1000: (d) pH (no SS1000 was added into the solution as a control group), (e) co-existing anions and HA (the concentration of HA was 10 mg·L^{-1} and 100 mg·L^{-1}), (f) SS1000 dosage, (g) different water matrices, and (h) reusability cycles.

removal efficiency of TCEP on SS1000, and even when the HA concentration was as high as 100 mg·g^{-1}, only a slight inhibition (Q_e> 50 mg·g^{-1}) was observed, indicating that natural organic substances in water have less influence on the adsorption of TCEP on SS1000.

In addition, the effect of SS1000 dosage on the adsorption efficiency of TCEP was also investigated in this study (Fig. 3f). When the adsorbent dosage was raised from 0.05 g·L^{-1} to 0.20 g·L^{-1}, the adsorption efficiency of TCEP increased from 36.22% to 95.86%. In order to test the application potential of the adsorbent (Fig. 3g and Table S5), the TCEP in three different water matrices including groundwater, river water and

dye effluent (the correlative water quality is shown in Tables S6-S8) was used as feed solution. When groundwater was used, the performance of SS1000 on the TCEP removal was negligibly affected, confirming the applicability of the SS1000 in groundwater remediation. In contrast, the inhibition of TCEP removal was observed when dye effluent and river water were used. The more noticeable interference caused by dye effluent might be owing to the presence of high-concentration dissolved organic compounds or other substances, which can compete adsorption sites with TCEP (Dou et al., 2022; Liu et al., 2020). The SS1000 exhibits a high removal efficiency for other organic pollutants such as TPhP, BPA and TBBPA (Fig. S3 and Table S9). The removal efficiency of the above-mentioned pollutants on SS1000 follows the order: TCEP > BPA > TBBPA > TPhP. The stronger affinity of BPA toward the SS1000 than TBBPA and TPhP can be attributing to the higher octanol-water partition coefficient (log D_{OW}) of BPA, which can enhance its hydrophobic interaction with SS1000 (Wu et al., 2019).

The reusability and regeneration performance of SS1000 were evaluated through a series of adsorption-desorption cycle experiments. In the first two cycles, the absorbed SS1000 was regenerated with ethanal (10 wt%) and used for the next adsorption process. As shown in Fig. 3h, the TCEP removal efficiency was reduced to 38.2% after two regeneration cycles. The spent adsorbent was then regenerated using ethanol (10 wt%) and 1.0 mol·L^{-1} NaOH, after which the TCEP removal efficiency of SS1000 improved to 44% again, indicating that the reusability of SS1000 further improved by searching for more suitable regeneration reagents. Not only that, it should be mentioned that of all the studied materials, SS1000 showed the best maximum adsorption capacity (Q_{max}) for TCEP adsorption (Table S10).

3.4. Mechanisms elucidation of SSs in removing TCEP

In previous studies, adsorbents with higher specific surface area and richer pore structure tended to adsorb pollutants better (Cai et al., 2021; He et al., 2020; Yu et al., 2022). However, the TCEP adsorption on our prepared biochar seems to be independent of its specific surface area and pore structure. Since the TCEP adsorption on the adsorbent is controlled by the chemosorption process, the interaction between TCEP and the functional groups or chemical components on biochar should be discussed to better understand the TCEP adsorption mechanism. Based on the XRD and FT-IR analysis, the prepared biochar contained Ca crystals including CaO, $CaCO_3$ and $Ca(OH)_2$. In addition, more Ca crystals were precipitated on the surface of SS1000. During the adsorption, Ca may be the binding sites for the TCEP adsorption, and the dissolved Ca^{2+} can also act as electrolytes to promote the adsorption of TCEP by SS1000.

In order to verify the role of Ca^{2+} in the TCEP adsorption, Ca^{2+} ions with a concentration of 100 mM were introduced into the TCEP solutions. As illustrated in Fig. 4a, when 100 mM Ca^{2+} ions were added alone or pH was adjusted to 9.0, the removal rates of TCEP were only 0.58% and 5.91%, suggesting that the salinity or self-hydrolysis effect was insufficient to effectively remove TCEP from water. However, when SS1000 was added to the system, the removal performance was significantly improved. When the "SS1000 + 100 mM Ca^{2+} + pH = 9″ system was formed, the removal of TCEP improved significantly from 63.67% to 84.08%, indicating that Ca^{2+} ions could promote the adsorption of TCEP on SS1000 under basic condition. The spectra of FT-IR and XPS were employed for the elucidation of SS1000 in removing TCEP. As shown in Fig. 4b, several obvious differences are observed for SS1000 after TCEP adsorption. The band at 3674 cm^{-1} (assigned to stretching vibration of

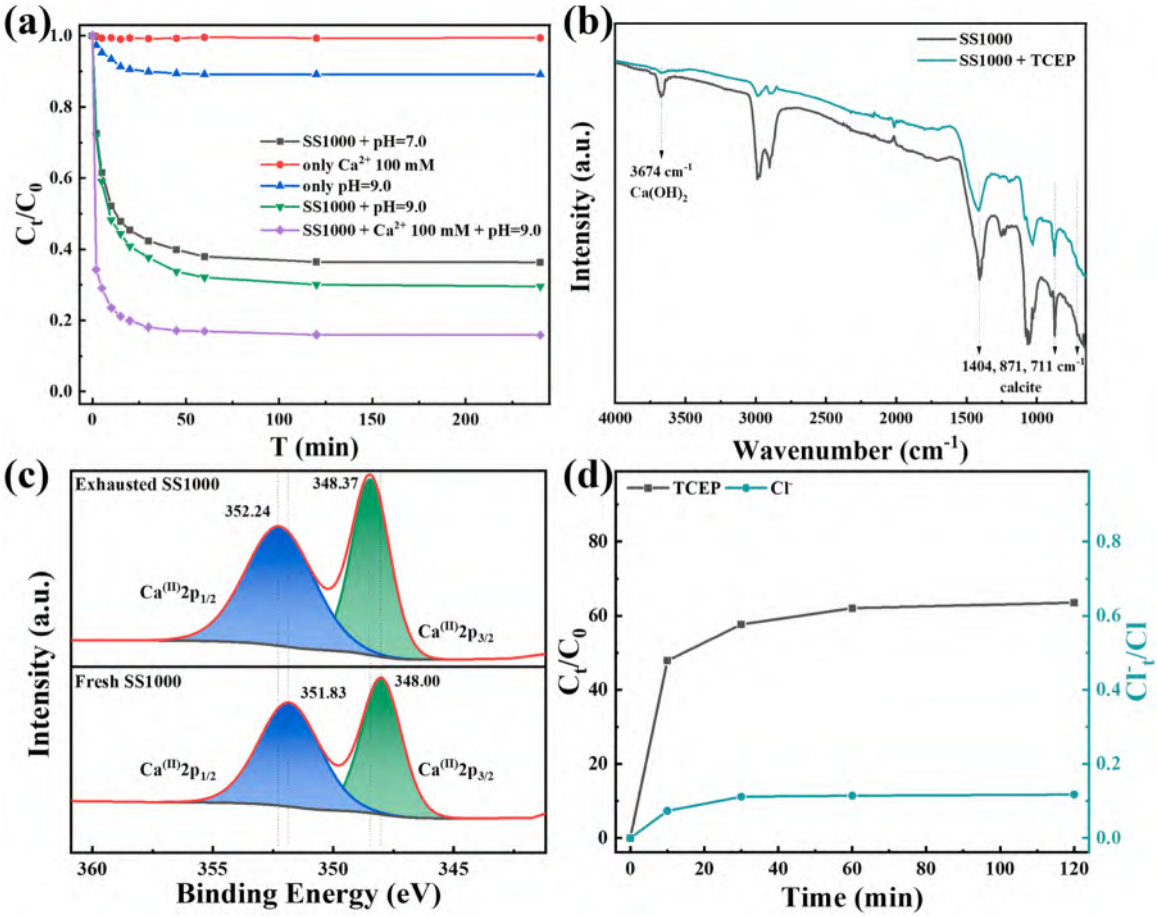

Fig. 4. (a) Effect of calcium and solution basicity. (b) FT-IR and (c) XPS spectra of Ca 2p of SS1000 before and after the adsorption. (d) Change of Cl^- concentration during the adsorption.

O-H in $Ca(OH)_2$) nearly disappeared after the adsorption. Meanwhile, the intensity of typical bands at 1404, 871 and 711 cm^{-1} for calcite in SS1000 reduced obviously after the TCEP adsorption (Dai et al., 2018). The core-level Ca 2p XPS spectra of SS1000 before and after the reaction are reported in Fig. 4c. The peaks at 348.0 eV and 351.8 eV correspond to Ca^{2+} $2p_{3/2}$ and Ca^{2+} $2p_{1/2}$, respectively. After the TCEP adsorption, the Ca 2p peaks slightly shifted to the positions at higher binding energy, suggesting the formation of inner layer complexes (Ca-OP) (Li et al., 2021a; Onoda et al., 2002). Their results indicate that the mineral phase (calcite and Ca^{2+}) in SS1000 is highly involved in the TCEP adsorption process (Dai et al., 2017). Moreover, the TCEP adsorption capacity of SS1000 decreased seriously after pickling by acid before the adsorption (Fig. S4a). It is worthwhile to note that during the TCEP adsorption, the solution pH decreased rapidly in the first 30 min, which is consistent with the TCEP removal trend given in Fig. S4b. These demonstrates the key role of Ca species and basic functional groups in the removal of TCEP. To further understand the removal pathway of TCEP on the SS1000, the hydrolysate (BCEP, $m/z = 223.2$) generated in the reaction was analyzed by LC/MS (Liu et al., 2020; Yu et al., 2021), and the relevant mass spectra is shown in Fig. S5. By detecting the Cl^- concentration in solution during the TCEP adsorption process, the increase of Cl^- ions concentration was proportionate to the removal amount of TCEP from water as shown in Fig. 4d.

Based on the above results, the probable mechanism for TECP removal by SS1000 is proposed as below. Firstly, the TCEP was adsorbed on the surface of SS1000 and then converted to hydrolysate (BCEP) via the interaction with the basic functional groups on the biochar surface. Then, the calcium species (calcite and Ca^{2+}) in SS1000 can combine with BCEP to produce inner layer complexes (Ca-OP), which can further promote the hydrolysis of TCEP along with generate chlorine ions.

4. Conclusions

In this study, the biochar derived from shrimp shell was prepared to effectively remove TCEP from water. The surface morphology, specific surface area and calcium content could be highly affected by the carbonization temperature ranging from 600 to 1200 °C. The kinetics and isotherm studies showed that the TCEP adsorption on biochar could be better fitted by the pseudo-second-order and Langmuir isotherm models, indicating that the TCEP adsorption was controlled by chemosorption process. The maximum adsorption capacity of 264.11 $mg \cdot g^{-1}$ was achieved by SS1000 at pH 7.0. The SS1000 exhibited good and stable adsorption performance under different solution pH, co-existing anions and HA as well as water matrices. The SS1000 could be more effectively regenerated by using ethanol and NaOH. The mechanism study demonstrated that the basic functional groups and calcium species (calcite and Ca^{2+}) played key roles in the TCEP adsorption on SS1000. The calcium species on SS1000 surface can form inner layer complexes (Ca-OP) with TCEP and then promote the hydrolysis of TCEP. The prepared biochar can be considered as a suitable candidate for the effective removal of TCEP from water.

CRediT authorship contribution statement

Chenyu Yang: Data curation, Writing – original draft, Visualization. **Chang Liu**: Data curation, Formal analysis. **Yile Yan**: Writing – review & editing, Visualization. **Lun Lu**: Software. **Ruixue Ma**: Investigation. **Xian Xiao**: Supervision, Resources. **Yang Yu**: Writing – review & editing. **Yuan Zhao**: Resources. **Yujiang Yu**: Resources. **Liangzhong Li**: Conceptualization, Methodology, Project administration, Supervision.

Declaration of Competing Interest

The authors declare that they have no know competing financial interests or personal relationships that could have appeared to influence the work reported in this paper.

Data availability

Data will be made available on request.

Acknowledgments

The research was supported by the National Natural Science Foundation of China (42007390, 22006102), the Basic and Applied Basic Research Foundation of Guangdong Province (2021A1515010341, 2022A1515010346), the Science and Technology Program of Guangzhou, China (202201011626).

Appendix A. Supporting information

Supplementary data associated with this article can be found in the online version at doi:10.1016/j.ecoenv.2023.114728.

References

Abdullah, A.M., O'Shea, K.E., 2019. TiO2 photocatalytic degradation of the flame retardant tris (2-chloroethyl) phosphate (TCEP) in aqueous solution: A detailed kinetic and mechanistic study. J. Photochem. Photobiol. A-Chem. 377, 130–137. https://doi.org/10.1016/j.jphotochem.2019.03.026.

An, D., et al., 2017. Sustainability assessment of groundwater remediation technologies based on multi-criteria decision making method. Resour. Conserv. Recycl. 119, 36–46. https://doi.org/10.1016/j.resconrec.2016.08.002.

Cai, S., et al., 2021. Pyrrolic N-rich biochar without exogenous nitrogen doping as a functional material for bisphenol A removal: Performance and mechanism. Appl. Catal. B-Environ. 291, 120093–120102. https://doi.org/10.1016/j.apcatb.2021.120093.

Chingombe, P., et al., 2005. Surface modification and characterisation of a coal-based activated carbon. Carbon 43, 3132–3143. https://doi.org/10.1016/j.carbon.2005.06.021.

Choi, Y., Kim, S.D., 2021. Identification and Toxicity Prediction of Biotransformation Molecules of Organophosphate Flame Retardants by Microbial Reactions in a Wastewater Treatment Plant. Int. J. Mol. Sci. 22, 22105376. https://doi.org/10.3390/ijms22105376.

Dai, L.C., et al., 2017. Calcium-rich biochar from the pyrolysis of crab shell for phosphorus removal. J. Environ. Chem. Eng. 198, 70–74. https://doi.org/10.1016/j.jenvman.2017.04.057.

Dai, L.C., et al., 2018. Calcium-rich biochar from crab shell: An unexpected super adsorbent for dye removal. Bioresour. Technol. 267, 510–516. https://doi.org/10.1016/j.biortech.2018.07.090.

Dai, L.C., et al., 2021. Tuning oxygenated functional groups on biochar for water pollution control: A critical review. J. Hazard. Mater. 420, 126547–126559. https://doi.org/10.1016/j.jhazmat.2021.126547.

Dardouri, M., et al., 2018. Adsorption of cadmium (II), zinc (II) and iron (III) from water by new cross-linked reusable polystyrene adsorbents. Mater. Chem. Phys. 216, 435–445. https://doi.org/10.1016/j.matchemphys.2018.06.002.

van der Veen, I., de Boer, J., 2012. Phosphorus flame retardants: Properties, production, environmental occurrence, toxicity and analysis. Chemosphere 88, 1119–1153. https://doi.org/10.1016/j.chemosphere.2012.03.067.

Dou, J.B., et al., 2022. Biochar co-doped with nitrogen and boron switching the free radical based peroxydisulfate activation into the electron-transfer dominated nonradical process. Appl. Catal. B-Environ. 301, 120832–120843. https://doi.org/10.1016/j.apcatb.2021.120832.

Gerrity, D., et al., 2012. Development of surrogate correlation models to predict trace organic contaminant oxidation and microbial inactivation during ozonation. Water Res 46, 6257–6272. https://doi.org/10.1016/j.watres.2012.08.037.

Hamid, Y., et al., 2022. Functionalized biochars: Synthesis, characterization, and applications for removing trace elements from water. J. Hazard. Mater. 437, 129337–129360. https://doi.org/10.1016/j.jhazmat.2022.129337.

Han, J., et al., 2021. Spatiotemporal distribution and mass loading of organophosphate flame retardants (OPFRs) in the Yellow River of China (Henan segment. Environ. Pollut. 290, 118000–118008. https://doi.org/10.1016/j.envpol.2021.118000.

Hao, H., et al., 2020. Effects of tris (2-chloroethyl) phosphate (TCEP) on growth, reproduction and gene transcription in the protozoan Tetrahymena thermophila. Aquat. Toxicol. 222, 105477–105485. https://doi.org/10.1016/j.aquatox.2020.105477.

He, C., et al., 2020. Waste shrimp shell-derived hydrochar as an emergent material for methyl orange removal in aqueous solutions. Environ. Int. 134, 105340–105348. https://doi.org/10.1016/j.envint.2019.105340.

He, S., et al., 2022a. Identification and apportionment of shallow groundwater nitrate pollution in Weining Plain, northwest China, using hydrochemical indices, nitrate stable isotopes, and the new Bayesian stable isotope mixing model (MixSIAR. Environ. Pollut. 298, 118852–118862. https://doi.org/10.1016/j.envpol.2022.118852.

He, S., et al., 2022b. Predictive modeling of groundwater nitrate pollution and evaluating its main impact factors using random forest. Chemosphere 290, 133388–133398. https://doi.org/10.1016/j.chemosphere.2021.133388.

Ji, C., et al., 2023. In situ formed CaSO4 on waste dander biochar to inhibit the mineralization of soil organic carbon. Sci. Total Environ. 854, 158776–1587784. https://doi.org/10.1016/j.scitotenv.2022.158776.
Ji, W.C., et al., 2020. The adsorption of phosphate on hydroxylated alpha-SiO2 (001) surface and influence of typical anions: A theoretical study. Appl. Surf. Sci. 501, 144233–144241. https://doi.org/10.1016/j.apsusc.2019.144233.
Jiang, Y., et al., 2019. Migration and evolution of dissolved organic matter in landfill leachate-contaminated groundwater plume. Resour. Conserv. Recycl. 151, 104463–104471. https://doi.org/10.1016/j.resconrec.2019.104463.
Jin, J., et al., 2016. Properties of biochar-amended soils and their sorption of imidacloprid, isoproturon, and atrazine. Sci. Total Environ. 550, 504–513. https://doi.org/10.1016/j.scitotenv.2016.01.117.
Lee, S., et al., 2016. Occurrence and exposure assessment of organophosphate flame retardants (OPFRs) through the consumption of drinking water in Korea. Water Res 103, 182–188. https://doi.org/10.1016/j.watres.2016.07.034.
Lei, Y.X., et al., 2022. Co-ZIF reinforced cow manure biochar (CMB) as an effective peroxymonosulfate activator for degradation of carbamazepine. Appl. Catal. B-Environ. 319, 121932–121945. https://doi.org/10.1016/j.apcatb.2022.121932.
Lenters, V., et al., 2019. Early-life exposure to persistent organic pollutants (OCPs, PBDEs, PCBs, PFASs) and attention-deficit/hyperactivity disorder: A multi-pollutant analysis of a Norwegian birth cohort. Environ. Int. 125, 33–42. https://doi.org/10.1016/j.envint.2019.01.020.
Li, D., et al., 2021a. Reductive degradation of chlorinated organophosphate esters by nanoscale zerovalent iron/cetyltrimethylammonium bromide composites: Reactivity, mechanism and new pathways. Water Res 188, 116447–116459. https://doi.org/10.1016/j.watres.2020.116447.
Li, J.H., et al., 2019. A review on organophosphate Ester (OPE) flame retardants and plasticizers in foodstuffs: Levels, distribution, human dietary exposure, and future directions. Environ. Int. 127, 35–51. https://doi.org/10.1016/j.envint.2019.03.009.
Li, L.Z., et al., 2021b. Rapid removal of thallium from water by a new magnetic nanocomposite using graphene oxide for efficient separation. Int. Biodeterior. Biodegrad. 161, 105245–105250. https://doi.org/10.1016/j.ibiod.2021.105245.
Li, N., et al., 2022. Municipal solid waste derived biochars for wastewater treatment: Production, properties and applications. Resour. Conserv. Recycl. 177, 106003–106018. https://doi.org/10.1016/j.resconrec.2021.106003.
Li, S.H., et al., 2021c. Seasonal concentration variation and potential influencing factors of organophosphorus flame retardants in a wastewater treatment plant. Environ. Res. 199, 111318–111325. https://doi.org/10.1016/j.envres.2021.111318.
Liang, Y., et al., 2018. Measuring and modeling surface sorption dynamics of organophosphate flame retardants on impervious surfaces. Chemosphere 193, 754–762. https://doi.org/10.1016/j.chemosphere.2017.11.080.
Liu, B.M., et al., 2020. Enhanced removal of tris(2-chloroethyl) phosphate using a resin-ased nanocomposite hydrated iron oxide through a Fenton-like process: Capacity evaluation and pathways. Water Res 175, 115655–115668. https://doi.org/10.1016/j.watres.2020.115655.
Long, L., et al., 2017. Synthesis, characterization and mechanism analysis of modified crayfish shell biochar possessed ZnO nanoparticles to remove trichloroacetic acid. J. Clean. Prod. 166, 1244–1252. https://doi.org/10.1016/j.jclepro.2017.08.122.
Luo, Y.L., et al., 2014. A review on the occurrence of micropollutants in the aquatic environment and their fate and removal during wastewater treatment. Sci. Total Environ. 473, 619–641. https://doi.org/10.1016/j.scitotenv.2013.12.065.
Mathew, G.M., et al., 2020. Sustainable and eco-friendly strategies for shrimp shell valorization. Environ. Pollut. 267, 155656–155670. https://doi.org/10.1016/j.envpol.2020.115656.
Mironyuk, I., et al., 2019. Highly efficient adsorption of strontium ions by carbonated mesoporous TiO2. J. Mol. Liq. 285, 742–753. https://doi.org/10.1016/j.molliq.2019.04.111.
Onoda, A., et al., 2002. Mononuclear Ca(II)-bulky aryl-phosphate monoanion and dianion complexes with ortho-amide groups. Inorg. Chem. 41, 6038–6047. https://doi.org/10.1021/ic010570f.
Reemtsma, T., et al., 2008. Organophosphorus flame retardants and plasticizers in water and air I. Occurrence and fate. Trac-Trends. Anal. Chem. 27, 727–737. https://doi.org/10.1016/j.trac.2008.07.002.
Sala, B., et al., 2019. First determination of high levels of organophosphorus flame retardants and plasticizers in dolphins from Southern European waters. Environ. Res. 172, 289–295. https://doi.org/10.1016/j.envres.2019.02.027.
Sunderland, E.M., et al., 2019. A review of the pathways of human exposure to poly- and perfluoroalkyl substances (PFASs) and present understanding of health effects. J. Expo. Sci. Environ. Epidemiol. 29, 131–147. https://doi.org/10.1038/s41370-018-0094-1.
Tang, X.D., et al., 2021. Extremely efficient and rapidly adsorb methylene blue using porous adsorbent prepared from waste paper: Kinetics and equilibrium studies. J. Hazard. Mater. 402, 123579–123592. https://doi.org/10.1016/j.jhazmat.2020.123579.
Tian, W.J., et al., 2022. Effects of pine sawdust and shrimp shell biochar on anaerobic digestion under different acidification conditions. J. Environ. Chem. Eng. 10, 106581–106591. https://doi.org/10.1016/j.jece.2021.106581.
Tong, X., et al., 2020. Function of agricultural waste montmorillonite-biochars for sorptive removal of 17 beta-estradiol. Bioresour. Technol. 296, 122368–122375. https://doi.org/10.1016/j.biortech.2019.122368.
Tripathy, S.S., Kanungo, S.B., 2005. Adsorption of Co2+, Ni2+, Cu2+ and Zn2+ from 0.5 M NaCl and major ion sea water on a mixture of delta-MnO2 and amorphous FeOOH. J. Colloid Interface Sci. 284, 30–38. https://doi.org/10.1016/j.jcis.2004.09.054.
Tseng, M.L., et al., 2022. Causality of circular business strategy under uncertainty: A zero-waste practices approach in seafood processing industry in Vietnam. Resour. Conserv. Recycl. 181, 106263–106282. https://doi.org/10.1016/j.resconrec.2022.106263.
Wu, L.P., et al., 2018. Characterizing chemical transformation of organophosphorus compounds by C-13 and H-2 stable isotope analysis. Sci. Total Environ. 615, 20–28. https://doi.org/10.1016/j.scitotenv.2017.09.233.
Wu, P.F., et al., 2019. Adsorption mechanisms of five bisphenol analogues on PVC microplastics. Sci. Total Environ. 650, 671–678. https://doi.org/10.1016/j.scitotenv.2018.09.049.
Xiao, Y.L., et al., 2017. Sorption of heavy metal ions onto crayfish shell biochar: Effect of pyrolysis temperature, pH and ionic strength. J. Taiwan Inst. Chem. Eng. 80, 114–121. https://doi.org/10.1016/j.jtice.2017.08.035.
Ye, S.J., et al., 2020. Nitrogen-doped biochar fiber with graphitization from Boehmeria nivea for promoted peroxymonosulfate activation and non-radical degradation pathways with enhancing electron transfer. Appl. Catal. B-Environ. 269, 118850–118860. https://doi.org/10.1016/j.apcatb.2020.118850.
Yu, X.L., et al., 2021. Photocatalysis of Tris-(2-chloroethyl) phosphate by ultraviolet driven peroxymonosulfate oxidation process: Removal performance, energy evaluation and toxicity on bacterial metabolism network. Chem. Eng. J. 423, 130261–130270. https://doi.org/10.1016/j.cej.2021.130261.
Yu, Y.J., et al., 2022. One-step synthesized iron-carbon core-shell nanoparticles to activate persulfate for effective degradation of tetrabromobisphenol A: performance and activation mechanism. Nanomaterials 12, 12244483. https://doi.org/10.3390/nano12244483.
Zafar, F.F., et al., 2022. Highly efficient adsorption of Bisphenol A using $NaHCO_3/CO_2$ activated carbon composite derived from shrimp shell@cellulose. Environ. Sci. Pollut. Res. 29, 68724–68734. https://doi.org/10.1007/s11356-022-20564-9.
Zhang, H.H., et al., 2022. Insight into the adsorption isotherms and kinetics of Pb (II) on pellet biochar via in-situ non-destructive 3D visualization using micro-computed tomography. Bioresour. Technol. 358, 127406–127412. https://doi.org/10.1016/j.biortech.2022.127406.
Zhang, Q., et al., 2021. Spatial occurrence and composition profile of organophosphate esters (OPEs) in farmland soils from different regions of China: Implications for human exposure. Environ. Pollut. 276, 116729–116738. https://doi.org/10.1016/j.envpol.2021.116729.
Zheng, H.Y., et al., 2022. Terrigenous export and ocean currents' diffusion of organophosphorus flame retardants along China's adjacent seas. Environ. Pollut. 299, 118873–118881. https://doi.org/10.1016/j.envpol.2022.118873.
Zhou, X.Y., et al., 2020. Biotransformation of Tris(2-chloroethyl) Phosphate (TCEP) in Sediment Microcosms and the Adaptation of Microbial Communities to TCEP. Environ. Sci. Technol. 54, 5489–5497. https://doi.org/10.1021/acs.est.9b07042.
Zhou, Y.Z., et al., 2018. Adsorption of Congo red from aqueous solution onto shrimp shell powder. Adsorpt. Sci. Technol. 36, 1310–1330. https://doi.org/10.1177/0263617418768945.
Zhu, K.R., et al., 2022. Occurrence, distribution and risk assessment of organophosphate esters (OPEs) in water sources from Northeast to Southeast China. Environ. Pollut. 307, 119461–119467. https://doi.org/10.1016/j.envpol.2022.119461.